



Co-synthesis of zirconium boride/silicide/oxide composite powders by magnesiothermic reduction

Didem Ovalı-Döndaş ^{1,*}

¹Osmaniye Korkut Ata University, Department of Mechanical Engineering, Osmaniye, 80000, Türkiye

ARTICLE INFO

Article history:

Received September 20, 2022

Accepted December 1, 2022

Available online December 31, 2022

Research Article

DOI: 10.30728/boron.1177551

Keywords:

ZrB₂

ZrSi

High-energy ball milling

Magnesiothermic reduction

X-ray diffraction

ABSTRACT

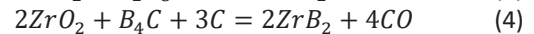
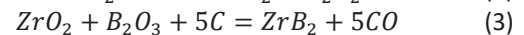
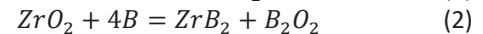
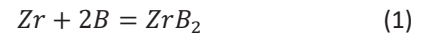
This study uses a magnesiothermic reduction method to investigate the co-synthesis of zirconium boride, silicides, and oxide powder composites using ZrO₂, B₂O₃, Si, and Mg powders. Synthesis of high-temperature ceramic powders was examined through milling durations, reduction temperatures, and excess magnesium addition. Thermochemical analysis of probable reaction products was conducted by the Factsage software. According to the results, the thermochemical predictions and resultant powder phases showed good coherency. High-energy milling has a significant effect on the formation of the zirconium boride phase after annealing. However, extended milling time and higher annealing temperature had no significant effect on composition of the constituted composite powders according to the X-ray diffraction results. An annealing temperature of 600°C was enough to obtain ZrB₂-based ceramic composite powders. In the final powder phases, the excess magnesium addition to the stoichiometric displays an important feature. After the milling, annealing, and leaching procedure, the stoichiometric powder composition comprises ZrB₂, ZrSi, ZrSi₂, ZrO₂, and MgSiO₂, and excess Mg added powders have the ZrB₂, ZrSi, ZrSi₂, ZrO₂ phases in their structure. Scanning electron microscopy analysis was utilized to observe the morphologies of the powders throughout each step of the synthesis procedure and revealed the finely structured morphology of synthesized powders.

1. Introduction

Ultra high-temperature ceramics (UHTCs) are well known for their extreme resistance in high-temperature environments and their melting temperatures above 3000°C [1, 2]. Different borides, nitrides, carbides, and silicides of IV and V group elements in the periodic table have gained recognition of UHTC. Their common advanced properties are high thermal conductivity, high hardness, low coefficient of thermal expansion, good thermal shock resistance, good oxidation resistance, and stability in extreme environments [3]. One of them, zirconium borides, has been seen as a promising compound for different applications as cutting tools, wear-resistant coatings, hypersonic flights, and rocket propulsion systems. Therefore, researchers have published many works about synthesizing or applying zirconium boride-based materials because of their supreme properties [4].

Zirconium-boron binary phase diagram presents three different crystal structures of zirconium boride as ZrB (stable up to 927°C), ZrB₁₂ (stable between 1720-2030°C), and ZrB₂ (stable up to 3227°C) [5]. The synthesis of zirconium boride is possible in many methods using high-temperature reactions, including elemental

Zr and B powder. The zirconium borides are commonly obtained through high-temperature methods such as the direct reaction of elemental powders (Eq.1), borothermal (Eq.2), and carbothermal (Eq.3 and Eq.4) reduction of ZrO₂ [4, 6]. However, the synthesis process of ZrB₂ from elemental powders cannot be commercially produced because of the expensive charge materials.



The production process of zirconium borides involves a high-temperature step over 1200°C due to their strong covalent bonding and low self-diffusion coefficient values. In order to enhance the structural integrity of zirconium borides, reinforcement materials were used as high-temperature borides, silicides, carbides, and oxides [7]. Especially, the initial powder conditions such as size, shape, and homogeneity play a critical role in the consolidation process and final properties of products [8]. On the other hand, aiming to obtain zirconium

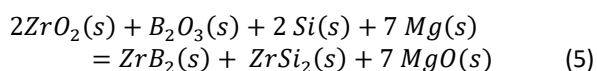
*Corresponding author: didemovali@osmaniye.edu.tr

boride composite powders could lead to a simplified synthesis process or a lowered annealing temperature for the reduction process of ZrO_2 . Therefore, many researchers conducted various works on the *in situ* synthesis of composites of zirconium boride together with other zirconium-based ceramic phases [1, 3, 9]. So far, ZrB_2 - ZrO_2 (Zirconium diboride-zirconium dioxide) [10-12], ZrB_2 - $ZrSi_2$ (Zirconium diboride-zirconium disilicite) [13-21], and ZrB_2 - ZrC (Zirconium diboride-zirconium carbide) [22, 23] binary systems were obtained using different starting compositions. Some of them resulted in ternary compositions such as $ZrSi_2$ - $MoSi_2$ - ZrB_2 [24], ZrB_2 - ZrC - SiC [25, 26], ZrB_2 - $ZrSi_2$ - SiC [27]. Having assessed the binary (e.g. boride-carbide) and ternary ceramic systems (e.g. boride-silicide-oxide), ternary systems could result in altered physical and mechanical properties due to their diverse microstructures [28]. And this may lead to the development of alternative materials for various applications. Among published papers about ternary ceramic systems, ZrB_2 - $ZrSi_2$ - ZrO_2 systems have not been attempted before, to our knowledge.

In this study, the synthesis of UHTC composite powders comprising zirconium boride/silicide/oxide was investigated through a magnesiothermic reduction process using ZrO_2 , B_2O_3 (Boron trioxide), Si, and Mg initials. Thermochemical software also examined the thermodynamic calculations for existence and probable by-products using initial batches. The synthesis procedures using ZrO_2 , B_2O_3 , Si, and Mg system were investigated in terms of different milling durations, excess Mg initial addition, and annealing temperatures. The outcomes of this study can contribute well to the existing literature for obtaining zirconium boride/silicide/oxide composite powders.

2. Materials and Methods

The initial materials were ZrO_2 (Alfa Aesar™, >99% purity), Si (ABCR™, >99% purity), Mg (Sigma Aldrich™, >99% purity), and B_2O_3 (Sigma Aldrich™, >99.9% purity) powders in this study. Each powder batch was calculated in Eq.5 and mixed in a Turbula blender for 2h.



Following Turbula blender, initial powder batches were subjected to high-energy ball milling (SPEX™ 8000D) for 3h, 6h, and 15h of milling durations. The initial powders were solely mixed using a blender mentioned as 0h. Hardened steel vials (50 ml capacity) and balls (6 mm Ø) were used and sealed under an Argon atmosphere. The ball-to-powder weight ratio (BPR) was 7:1 for each milling/run. The 0h, 3h, 6h, and 15h milled powders were placed in an alumina crucible and annealed in a Protherm™ tube furnace for 2h at various temperatures (600, 800, and 1000°C) under a flowing Ar atmosphere. The heating and cooling rates were

10°C/min for each run. The purification process of reacted powders was conducted using a dilute HCl solution (Merck™, 37% concentrated). The concentration and solid-to-liquid ratio of HCl solution were selected as 2 M and 1 g/10 ml, respectively. After centrifugation (Hettich™ Mikro 220/220R centrifuge, at 3500 rpm) for 20 min, decantation and filtration treatments were repeated three times, the powders were dried using an oven at 100°C.

Thermodynamic calculations were carried out using Factsage 7 thermochemical program. The FactPS database was used for thermodynamic calculations because of including all possible corresponding data in the gas, liquid, and solid phases. X-ray diffraction (XRD) patterns of powders were obtained using the Bruker™ D8 Advance Series X-ray diffractometer with $CuK\alpha$ (1.54Å) radiation. The morphological observations and microstructural characterization of powders were conducted using a FEI (Quanta FEG 250) scanning electron microscope (SEM) coupled with an energy-dispersive spectrometer (EDS). SEM analyses were operated at 15 kV under environmental mode.

3. Results and Discussion

The thermochemical predictions of the ZrO_2 - B_2O_3 -Si-Mg system were conducted by Factsage™ software to have a better understanding of the reaction probability and potential reaction products. The standard Gibbs free energy (ΔG°) and enthalpy (ΔH°) change of Eq.5 was calculated for different temperatures between 0 and 2000°C as given in Figures 1 (a) and (b), respectively. The large ΔG° and ΔH° values of Eq. 5 suggest that this reaction has a moral certainty. Figure 1(b) exhibits two sharp increase points in the ΔH° versus temperature curve at 630 and 1095°C which corresponds to the respective melting and boiling temperatures of Mg [29]. The ΔG° value of reaction (Eq.5) in Figure 1a shows a sharp increase around 1100°C caused by the vaporization of Mg.

Figure 1 pointed out that the reaction in Eq.5 could be started by a magnesiothermic reaction. Since our system has two oxides as ZrO_2 and B_2O_3 , the magnesiothermic reaction could progress as given in Eq.6 and 7.

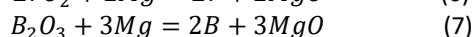
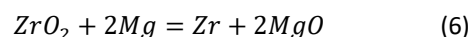


Figure 2 shows the probable reaction products predicted for varying amounts (from 0 to 15 mole) of magnesium input based on Eq.6. Below the stoichiometric mole of Mg (corresponds to 7 moles in Eq.6), the predicted reaction phases are ZrB_2 , $ZrSi$, MgO , Mg_2SiO_4 , $MgSiO_3$ together with residual ZrO_2 . According to the predictions, the Mg amount is below the stoichiometric proportion (7 moles for Mg), the reduction process of ZrO_2 and B_2O_3 dominates by the occurrence of silica (SiO_2) and silicate ($ZrSiO_4$, $MgSiO_3$, and Mg_2SiO_4) formations. The magnesiothermic reduction, as in Eq.2

and 3, takes place for a minimum of 3 moles of Mg. Above the stoichiometric proportion (7 moles of Mg) as in Eq.1, the only reduction mechanism is a magnesiothermic reaction, as understood by a sharp increase in the slope of the MgO curve in the graph (Figure 2). There is also a correlation between the initial Mg mole and magnesium silicate phases. When the amount of Mg addition increases, the $MgSiO_3$ curve decreases, and the Mg_2SiO_4 curve increases. The $MgSiO_3$ formations only exit up to three moles of Mg, which means the occurrence of Mg_2SiO_4 formations can be prevented with an increasing amount of Mg. In the stoichiometric

proportion (7 moles of Mg), the thermodynamic predictions point to the ZrSi, ZrB_2 , Mg_2SiO_4 , and MgO phases. This result indicates the existence of the ZrSi phase as possible instead of $ZrSi_2$ for all initial powder proportions, except stoichiometric ones. Therefore, both of ZrSi and $ZrSi_2$ phases could be obtained for our system based on the thermodynamic predictions. The increased initial Mg amount (especially 9 moles of Mg) contributes to the $ZrSi_2$ formation.

The XRD pattern of initial powders after various times of ball milling is illustrated in Figure 3. All XRD patterns infer the ZrO_2 (ICDD number: 01-078-0047, Primitive Monoclinic Bravais Lattice, P21/c), Si (ICDD number: 71-9399, Face-centered Cubic Bravais Lattice, Fd3m), and Mg (ICDD number: ICDD Card number: 27-1402, Bravais lattice: primitive hexagonal Bravais Lattice, P63/mmc) phases. The existence of B_2O_3 peaks is not detected in the XRD pattern due to its amorphous nature [10]. The peaks of ZrO_2 , Si, and Mg phases are broadened and their intensities are decreased by increasing high-energy milling durations. In addition to this, the ZrO_2 peak at 28.17° and Si peak at 28.42° in the XRD pattern of as-blended powders (referred to as 0 h) are overlapped by intense milling prolonged to 15h of milling. The main peak of Mg at 36.5° are drastically decreased by 3h and a longer time of milling, which is a good sign for the stored energy during milling. Since the reductive metal is magnesium in this study, the stored energy is an important indicator of a probable reaction during the annealing process [30].

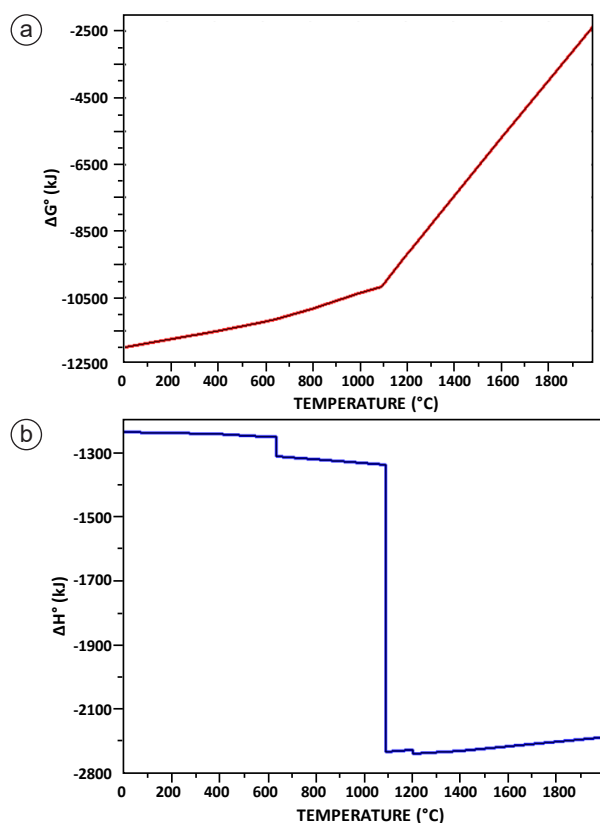


Figure 1. The graphs of (a) The ΔG° , and (b) ΔH° versus temperature based on Eq.5 were produced by the Factsage thermodynamic software.

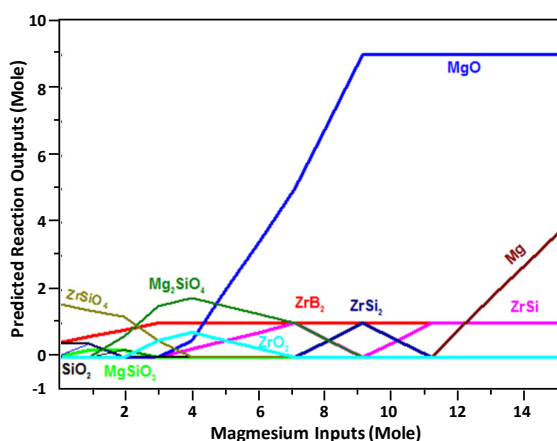


Figure 2. The amount of magnesium versus probable reaction products based on Eq.5 generated from the Factsage™ thermodynamic software.

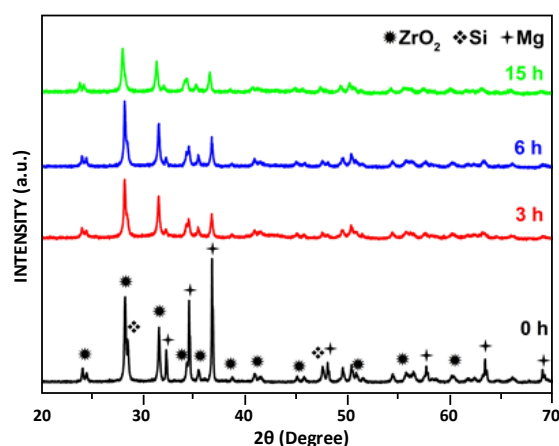


Figure 3. XRD patterns of high-energy ball-milled powders for 0h, 3h, 6h, and 15h.

XRD patterns of powders after various hours of high-energy milling and annealing at $600^\circ C$ are illustrated in Figure 4. The existing phases of as blended powders (addressed with 0h) are ZrO_2 (ICDD number: 01-078-0047, Primitive Monoclinic Bravais Lattice, P21/c), and Mg_2Si (ICDD number: 00-035-0773, Face-centered Cubic Bravais Lattice, Fm3m) with a small intensity peak of ZrB_2 (ICDD number: 01-089-3930, Primitive Hexagonal Bravais Lattice, P6/mmm). Since the XRD reflections of ZrO_2 have high intensities and there are small peaks belonging to ZrB_2 and MgO phases, it can

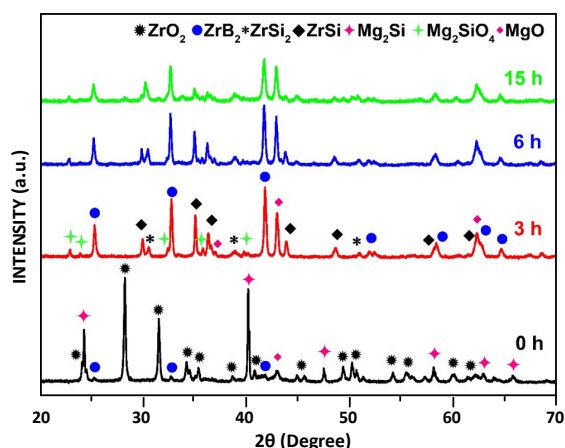


Figure 4. XRD patterns of high-energy ball milled powders for 0h, 3h, 6h, and 15h after annealing at 600°C for 2h.

be said that the magnesiothermic reduction of ZrO_2 slightly occurred. There are also no indications of a completed reduction in B_2O_3 at this stage. Therefore, it means the aimed reaction slightly takes place for the initial powder batch annealed at 600°C without milling. In the literature, the initial temperature for ZrB_2 phase formations in most synthesis studies starts above 800°C [10, 22, 26]. Some of them require extreme temperatures, such as 1650°C to obtain ZrB_2 formations synthesized from ZrO_2 and B_2O_3 initials [31, 32]. In this study, using ZrO_2 , B_2O_3 , Si, and Mg initials, the first formation temperature of the ZrB_2 phase was drawn up to 600°C. The XRD patterns of high-energy milled powders for 3, 6, and 15h (Figure 4) present mainly ZrB_2 (ICDD number: 01-078-0047, Primitive Monoclinic Bravais Lattice, P21/c), $ZrSi$ (ICDD number: 01-078-0047, Primitive Monoclinic Bravais Lattice, P21/c), $ZrSi_2$ (ICDD number: 01-078-0047, Primitive Monoclinic Bravais Lattice, P21/c), and MgO (ICDD number: 01-078-0047, Primitive Monoclinic Bravais Lattice, P21/c) phases together with a small intensity belonging to Mg_2SiO_4 . Since no peaks can be detected for ZrO_2 , it can be said that the magnesiothermic reduction completely occurred for high-energy milled powders. The zirconium silicide phase exists in two different stoichiometries as $ZrSi_2$ and $ZrSi$ compatible with thermodynamic prediction in Figure 2. The studies about synthesis of metal silicides showed it is quite possible to obtain metal silicide phases in a variety of stoichiometries especially the synthesis procedure involved a milling process [33, 34]. The thermodynamic predictions in Figure 2 also pointed to a possible Mg_2SiO_4 formation, as seen in the XRD patterns in Figure 4. A study revealed that the Mg_2SiO_4 phases easily formed with the initial powder batches containing Mg and Si phases [35]. Although zirconium boride and silicide phases were obtained for 3h milling and annealing, extended milling was applied up to 15h for the purpose of detecting any probable degradation or formation of a new phase. The peak intensities are slightly decreased by prolonged milling time, which suggests a decline in the crystallite size of powders based on the XRD patterns [30].

XRD patterns of high-energy ball milled powders annealed at 800°C and 1000°C are given in Figures 5a and b, respectively. The ZrB_2 , $ZrSi_2$, and $ZrSi$ phases are formed for 0h milled powders after annealing at 800°C and 1000°C. However, the existence of ZrO_2 and Si phases in the XRD pattern of 0h milled and annealed powders reveals the uncompleted reaction. With the effects of high-energy ball milling, the XRD patterns of annealed powders at 800°C and 1000°C reveal the reflections of ZrB_2 , $ZrSi_2$, $ZrSi$, and MgO structures together with a small one that arose from Mg_2SiO_4 phase. There is no distinguished difference between the XRD reflections of annealed powders at 600°C (Figure 4), 800°, and 1000°. It is understood that the structures formed in this study are stable and not affected by a higher temperature or an extended milling time. Since there is no significant difference, the minimum milling time (3h) and middle annealing temperature (800°C) can be described as optimum process conditions. In literature, most reaction temperatures to obtain the ZrB_2 phase from ZrO_2 and B_4C initials are above 1600°C [36]. With the help of milling, this reaction temperature was reduced to 1200°C [10]. Another study reduces the required annealing temperature to 800°C combining ZrO_2 with other elements/compounds such as Zr, B_4C , Si, and ZrC [26]. In this study, the ZrB_2 phase is obtained using ZrO_2 , B_2O_3 , Si, and Mg powders after the annealing process at 600°C with the help of milling. In a study, ZrB_2 powders were driven from ZrO_2 - B_2O_3 -Mg system by volume combustion synthesis method [37]. They stated the reaction temperature as 900°C. Comparing to initial systems, the reaction temperature was reduced to 600°C with addition of Si in this study.

A purification process with HCl acid solution was applied in order to remove the MgO phase from the powder structure synthesized via the magnesiothermic reduction. The XRD patterns of leached powders are given in Figures 6a and b. After purification, some undetected phases could be noticeable in the XRD patterns. For this reason, both 3h and 15h high-energy milled powders (annealed at 800°C) were leached. All peaks were sharp and had high intensities. After leaching, there is no new formation detected in the patterns. However, the undistinguishable ZrO_2 peaks in Figure 5a become clear view of the XRD patterns in Figure 6a and b. In another word, it is not possible to observe the ZrO_2 peaks detected at 28.5° and 31.5° because of its small intensity in Figure 5a (3h and 15h milled and annealed powders). The Figure 6b demonstrates that MgO phase is completely removed from powder structure by leaching. However, the Mg_2SiO_4 phase was remained in the powder structure because acid leaching could not eliminate it. By comparing the Figures 6a and b, it can be seen that the ZrO_2 peaks intensities of 3h milled powders are relatively higher than those in 15h milled powders, which suggests that milling causes a slight decrement in the residual ZrO_2 content. This can be attributed to the grain refinement caused by the fracture mechanism exposed during the

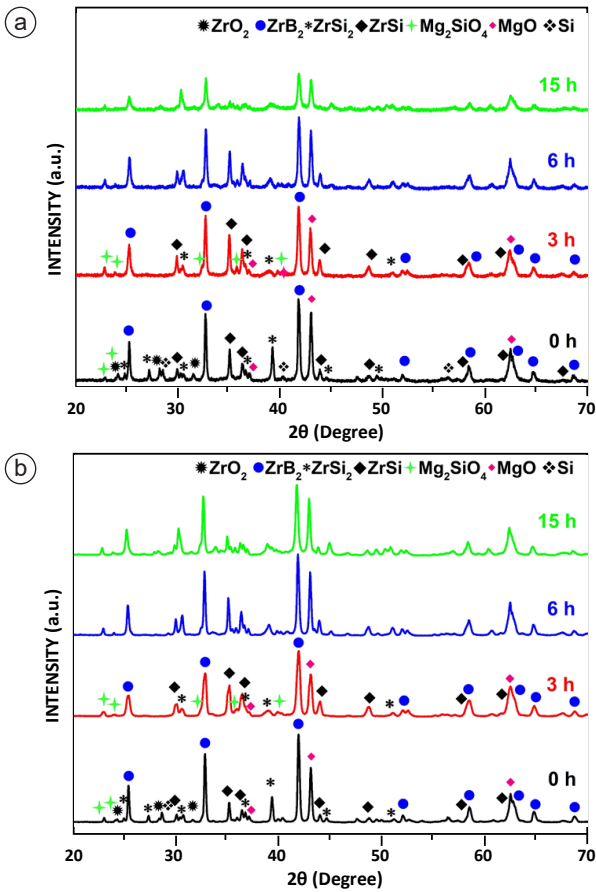


Figure 5. XRD patterns of high-energy ball milled powders for 0h, 3h, 6h, and 15h after annealing for 2h: a) at 800°C and b) at 1000°C.

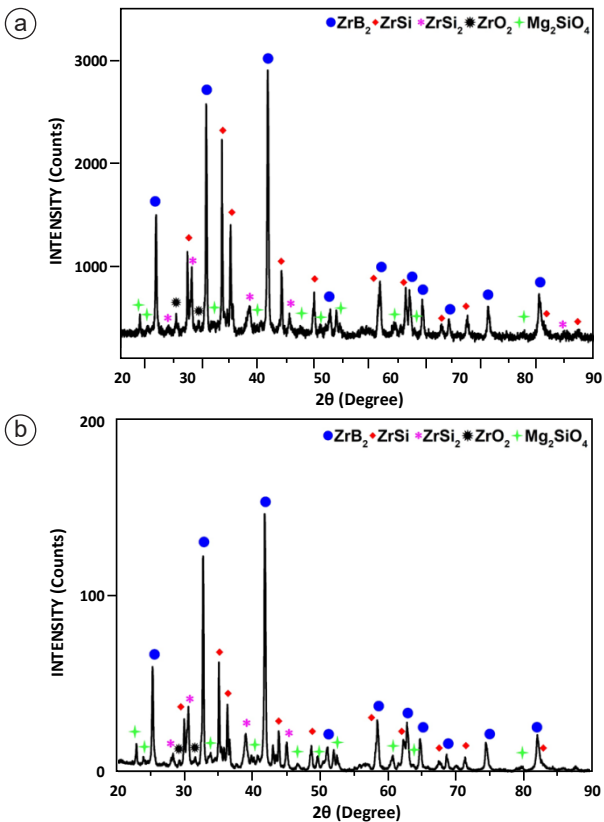


Figure 6. XRD pattern of powders after high-energy ball milled, annealed at 800°C, and leached powders: a) 3h MA and b) 15h MA.

milling process. These studies prove an excess Mg addition to the stoichiometric proportion can inhibit the $MgSiO_4$ formation during the synthesis procedure [33, 34]. Therefore, excess Mg added initial powder samples were milled for 3h and annealed at 800°C for 2h. Figure 7a and b presents the XRD analysis results of high-energy milled and annealed powders with excess Mg addition and those after leaching procedure, respectively. In the XRD pattern of milled and annealed powder, there are ZrB_2 , $ZrSi_2$, $ZrSi$, ZrO_2 , and MgO phases. After removing MgO phases by leaching, all peaks in the XRD pattern belong to ZrB_2 , $ZrSi_2$, $ZrSi$, and ZrO_2 phases. It is clear evidence for the inhibition of Mg_2SiO_4 formation by excess Mg addition. Comparing to Figure 6a, and 7b, there is a significant difference between the proportions of ZrB_2 , $ZrSi_2$, $ZrSi$ and ZrO_2 formations regarding to their peak intensities. For example, the reflections of $ZrSi_2$ in Figure 7b are quite higher than those in Figure 6b. Hence, it is obviously seen that excess Mg addition influences the zirconium boride, silicide and oxide phase composition in the synthesized powder structure. The XRD patterns of synthesized powder with excess Mg addition in Figure 7a present any reflection belonging to the residual Mg phase as unreacted initial if it is under the detection limit of XRD analysis. However, in the case of excess magnesium existence, the HCl leaching also removes it from the synthesized powder structure. Excess Mg addition attributes the $ZrSi_2$ occurrence instead of the $ZrSi$ phase. The thermodynamic predictions in Figure

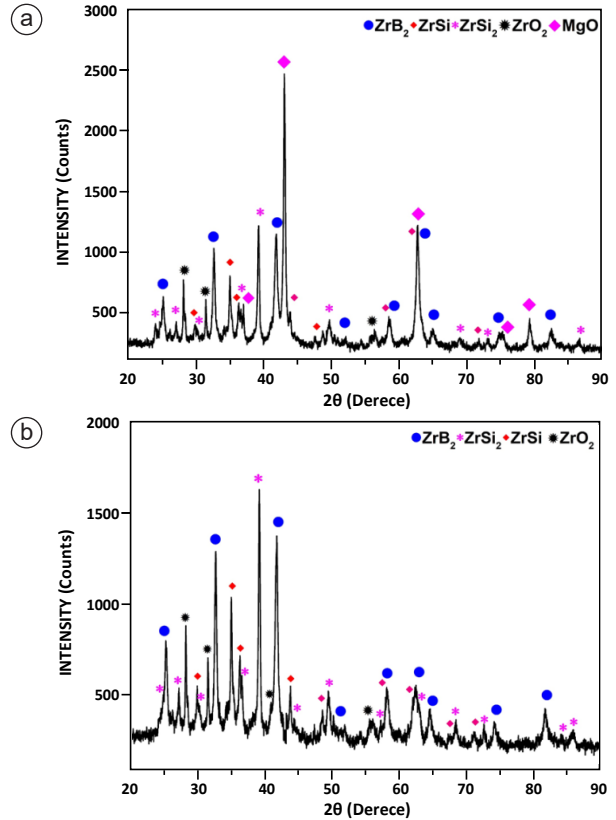


Figure 7. a) XRD pattern of excess Mg added powders after high-energy ball milling for 3h, annealing at 600°C and, b) those after leaching procedure.

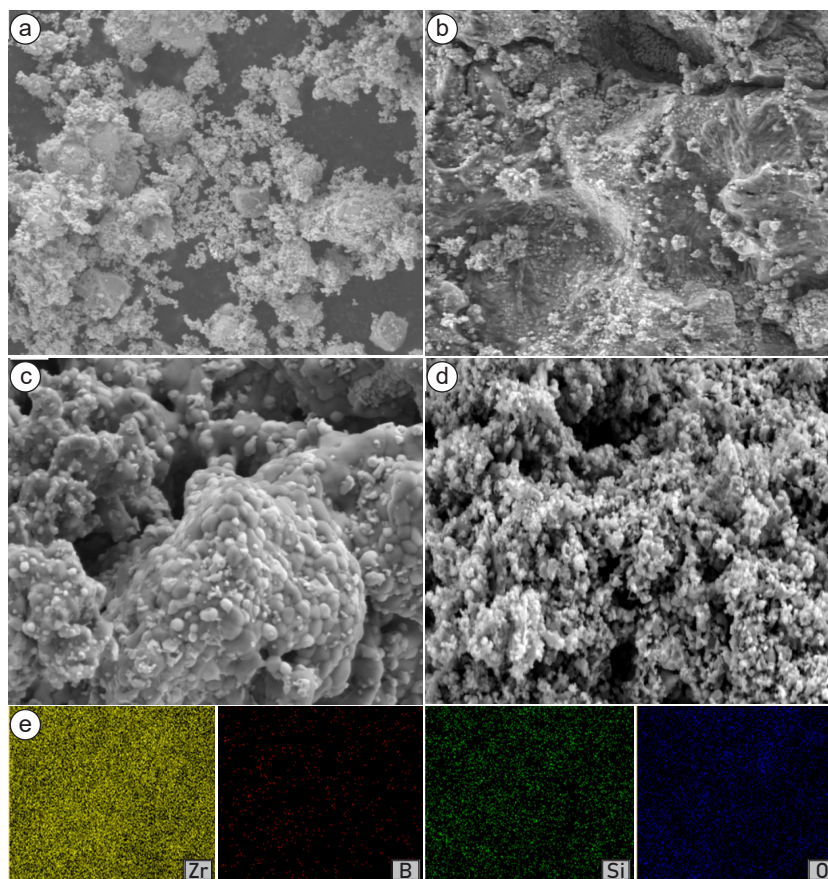


Figure 8. SEM images of excess Mg added powders: a) As-blended, b) High energy milled for 3h, c) High energy milled and annealed at 600°C, d) High energy milled, annealed at 600°C and leached, and e) Zr, B, Si and O elemental mapping of d.

2 show the constitution of $ZrSi_2$ formation rather than $ZrSi$ in the presence of excess Mg addition for 9 moles. The existence of $ZrSi$ is possible for other mole rates of Mg based on the Figure 2. Mg_2SiO_4 and $ZrSi_2$ phases have relation to the common Si content. Inhibition of Mg_2SiO_4 formation supports the formation of $ZrSi_2$ because there is more Si source to induce the existence of the zirconium silicide phase. Therefore, the $ZrSi$ phase exists in Figures 6 and 7 is probably originated from the residual of ZrO_2 . For solid state reactions, the initial powder composition plays a prominent role in the obtained powder embodi [38].

Figure 8 displays the secondary electron SEM images of excess Mg added powders. The as-blended powders placed in Figure 8a have irregular and different particle sizes presenting a homogenous morphology of ZrO_2 , B_2O_3 , Si, and Mg initials. The 3h milled particles, as seen in Figure 8b, have a uniform distribution. After annealing at 800°C for 2h, the zirconium boride/silicide/oxide particles are embedded into large agglomerated MgO particles. The leaching process provides the division of zirconium-based ceramic particles by dissolving the MgO phase in the HCl acid solution. Therefore, the SEM images of leached zirconium boride/silicide/oxide particles can be seen in Figure 8d. The synthesized zirconium-based ceramic particles have a spherical shape and their particle sizes are smaller than 0.5 μm , as seen in Figure 8d. The

elemental mapping of Zr, B, Si, and O conducted for zirconium boride/silicide/oxide particles was given in Figure 8e. The maps of Zr, B, Si, and O elements coincide almost entirely with each other, which suggests the presence and homogenous distribution of the zirconium boride, silicide, and oxide phases.

4. Conclusions

Milling, annealing and following leaching process of the ZrO_2 , B_2O_3 , Si and Mg were successfully used in the fabrication of zirconium boride/silicide/oxide ceramic powders with fine microstructure. Synthesis procedure was studied in terms of different milling duration, annealing temperature and excess Mg addition. The results of experimental studies and thermodynamic analysis are compatible with each other regarding the formation of probable phases. The formation of ZrB_2 starts after milling for 3h and annealing at 600°C. Results showed that the application of milling has significant effects on the resultant composition; however, further milling and different annealing temperatures displayed any determinant difference. The ZrB_2 , $ZrSi_2$, $ZrSi$, ZrO_2 and Mg_2SiO_4 phases were obtained using the stoichiometric proportion of initial powders after the synthesis and purification process. Applying excess Mg addition to the stoichiometric proportion, the occurrence of Mg_2SiO_4 formation was prevented and the final structure of powders comprised ZrB_2 , $ZrSi_2$,

ZrSi and ZrO₂ phases based on the XRD results. The SEM analysis showed the powder products have homogenous distribution and fine structure.

Acknowledgement

The author wishes to express her gratitude to Prof. Dr. Lütfi Öveçoğlu for permission of using the Particulate Materials Laboratory infrastructure for milling and XRD analyses. The author thanks to Assoc. Prof. Dr. Nazlı Akçamlı for thermodynamic analysis. The author acknowledges the Namık Kemal University Center Laboratory (NABİLTEM) for conducting SEM analysis.

References

- [1] Golla, B. R., Mukhopadhyay, A., Basu, B., & Thimmappa, S. K. (2020). Review on ultra-high temperature boride ceramics. *Progress in Materials Science*, 111, 100651.
- [2] Zhang, G. J., Ni, D. W., Zou, J., Liu, H. T., Wu, W. W., Liu, J. X., ... & Sakka, Y. (2018). Inherent anisotropy in transition metal diborides and microstructure/property tailoring in ultra-high temperature ceramics-A review. *Journal of the European Ceramic Society*, 38(2), 371-389.
- [3] Sonber, J. K., & Suri, A. K. (2011). Synthesis and consolidation of zirconium diboride: review. *Advances in Applied Ceramics*, 110(6), 321-334.
- [4] Fahrenholtz, W. G., Hilmas, G. E., Talmy, I. G., & Zaykoski, J. A. (2007). Refractory diborides of zirconium and hafnium. *Journal of the American Ceramic Society*, 90(5), 1347-1364.
- [5] Predel B (2012) *B - Zr (Boron - Zirconium)* (Vol. 12B, pp 87-88). In: Predel B (Ed.). Springer.
- [6] Karasev, A. I. (1973). Preparation of technical zirconium diboride by the carbothermic reduction of mixtures of zirconium and boron oxides. *Soviet Powder Metallurgy and Metal Ceramics*, 12(11), 926-929.
- [7] Zhu, S., Fahrenholtz, W. G., & Hilmas, G. E. (2007). Influence of silicon carbide particle size on the microstructure and mechanical properties of zirconium diboride-silicon carbide ceramics. *Journal of the European Ceramic Society*, 27(4), 2077-2083.
- [8] Ağaoğulları, D., Balcı, Ö., Mertdinç, S., Tekoğlu, E., & Öveçoğlu, M. L. (2018). Synthesis of VB₂-V₃B₄-V₂B₃/VC hybrid powders via powder metallurgy processes. *Journal of Boron*, 3(3), 180-187.
- [9] Aguirre, T. G., Lamm, B. W., Cramer, C. L., & Mitchell, D. J. (2022). Zirconium-diboride silicon-carbide composites: A review. *Ceramics International*, 48(6), 7344-7361.
- [10] Balcı, Ö., Ağaoğulları, D., Duman, İ., & Öveçoğlu, M. L. (2012). Carbothermal production of ZrB₂-ZrO₂ ceramic powders from ZrO₂-B₂O₃/B system by high-energy ball milling and annealing assisted process. *Ceramics International*, 38(3), 2201-2207.
- [11] Balcı, Ö., Akçamlı, N., Ağaoğulları, D., Öveçoğlu, M. L., & Duman, İ. (2017). Otoklavda sentezlenen ZrB₂-ZrO₂ tozlarının farklı tekniklerle sinterlenmesi ve yığın yapılarının mikroyapısal ve bazı mekanik özelliklerinin incelenmesi. *Journal of Boron*, 2(1), 1-10.
- [12] Xu, L., Guo, W., Liu, Q., Zhang, Y., Wu, L., You, Y., & Lin, H. (2022). Fully dense ZrB₂ ceramics by borothermal reduction with ultra-fine ZrO₂ and solid solution. *Journal of the American Ceramic Society*, October 2021, 1-8.
- [13] Sha, J. J., Wei, Z. Q., Li, J., Zhang, Z. F., Yang, X. L., Zhang, Y. C., & Dai, J. X. (2014). Mechanical properties and toughening mechanism of WC-doped ZrB₂-ZrSi₂ ceramic composites by hot pressing. *Materials and Design*, 62, 199-204.
- [14] Yen, B. K. (1998). X-ray diffraction study of mechanochemical synthesis and formation mechanisms of zirconium carbide and zirconium silicides. *Journal of Alloys and Compounds*, 268(1-2), 266-269.
- [15] Silvestroni, L., Meriggi, G., & Sciti, D. (2014). Oxidation behavior of ZrB₂ composites doped with various transition metal silicides. *Corrosion Science*, 83, 281-291.
- [16] Zamora, V., Guiberteau, F., & Ortiz, A. L. (2020). Effect of high-energy ball-milling on the spark plasma sinterability of ZrB₂ with transition metal disilicides. *Journal of the European Ceramic Society*, 40(15), 5020-5028.
- [17] Wang, M., Wang, C. A., & Zhang, X. (2012). Effects of SiC platelet and ZrSi₂ additive on sintering and mechanical properties of ZrB₂-based ceramics by hot-pressing. *Materials and Design*, 34, 293-297.
- [18] Sha, J. J., Li, J., Wang, S. H., Wang, Y. C., Zhang, Z. F., & Dai, J. X. (2015). Toughening effect of short carbon fibers in the ZrB₂-ZrSi₂ ceramic composites. *Materials and Design*, 75, 160-165.
- [19] Guo, S. Q., Kagawa, Y., Nishimura, T., & Tanaka, H. (2008). Pressureless sintering and physical properties of ZrB₂-based composites with ZrSi₂ additive. *Scripta Materialia*, 58(7), 579-582.
- [20] Guo, S. Q. Q., Kagawa, Y., & Nishimura, T. (2009). Mechanical behavior of two-step hot-pressed ZrB₂-based composites with ZrSi₂. *Journal of the European Ceramic Society*, 29(4), 787-794.
- [21] Jia, Y., Mehta, S. T., Li, R., Chowdhury, M. A. R., Horn, T., & Xu, C. (2021). Additive manufacturing of ZrB₂-ZrSi₂ ultra-high temperature ceramic composites using an electron beam melting process. *Ceramics International*, 47(2), 2397-2405.
- [22] Mousavi, S. M., Zakeri, M., Kermani, M., Rahimipour, M. R., & Tayebifard, S. A. (2019). A comparative study on the synthesis of oxide-free ZrB₂-xZrC composites. *Ceramics International*, 45(3), 3760-3766.
- [23] Adibpur, F., Zaferi, M., & Tayebifard, S. A. (2013). Feasibility study of metallic reductant element replacement by mechanical activation process in ZrB₂-ZrC composite synthesis from raw oxide materials by SHS. *Life Science Journal*, 10(8s), 336-341.
- [24] Astapov, A. N., Pogozhev, Y. S., Prokofiev, M. V., Lifanov, I. P., Potanin, A. Y., Levashov, E. A., & Vershinnikov, V. I. (2019). Kinetics and mechanism of high-temperature oxidation of the heterophase ZrSi₂-MoSi₂-ZrB₂ ceramics. *Ceramics International*, 45(5), 6392-6404.
- [25] Liu, C., Chang, X., Wu, Y., Li, X., Xue, Y., Wang, X., & Hou, X. (2020). In-situ synthesis of ultra-fine ZrB₂-ZrC-SiC

- nanopowders by sol-gel method. *Ceramics International*, 46(6), 7099-7108.
- [26] Qu, Q., Han, J., Han, W., Zhang, X., & Hong, C. (2008). In situ synthesis mechanism and characterization of ZrB₂-ZrC-SiC ultra high-temperature ceramics. *Materials Chemistry and Physics*, 110(2-3), 216-221.
- [27] Shao, G., Zhao, X., Wang, H., Chen, J., Zhang, R., Fan, B., ... & Chen, D. (2016). ZrB₂-ZrSi₂-SiC composites prepared by reactive spark plasma sintering. *International Journal of Refractory Metals and Hard Materials*, 60, 104-107.
- [28] Liu, H. L., Liu, J. X., Liu, H. T., & Zhang, G. J. (2015). Contour maps of mechanical properties in ternary ZrB₂-SiC-ZrC ceramic system. *Scripta Materialia*, 107, 140-144.
- [29] Ağaoğulları, D., Balcı, Ö., Akçamlı, N., Suryanarayana, C., Duman, İ., & Öveçoğlu, M. L. (2019). Mechanochemical synthesis and consolidation of nanostructured cerium hexaboride. *Processing and Application of Ceramics*, 13(1), 32-43.
- [30] Balcı, Ö., Ağaoğulları, D., Ovalı, D., Öveçoğlu, M. L., & Duman, İ. (2015). In situ synthesis of NbB₂-NbC composite powders by milling-assisted carbothermal reduction of oxide raw materials. *Advanced Powder Technology*, 26(4), 1200-1209.
- [31] Baris, M., Simsek, T., Simsek, T., Ozcan, S., & Kalkan, B. (2018). High purity synthesis of ZrB₂ by a combined ball milling and carbothermal method: Structural and magnetic properties. *Advanced Powder Technology*, 29(10), 2440-2446.
- [32] Ran, S., Van der Biest, O., & Vleugels, J. (2010). ZrB₂ powders synthesis by borothermal reduction. *Journal of the American Ceramic Society*, 93(6), 1586-1590.
- [33] Ovalı, D., Ağaoğulları, D., & Öveçoğlu, M. L. (2019). Mechanochemical synthesis and characterisation of niobium silicide nanoparticles. *Ceramics International*, 45(8), 10654-10663.
- [34] Ovalı, D., Ağaoğulları, D., & Öveçoğlu, M. L. (2017). Effects of excess reactant amounts on the mechanochemically synthesized molybdenum silicides from MoO₃, SiO₂ and Mg blends. *International Journal of Refractory Metals and Hard Materials*, 65, 19-24.
- [35] Ovalı, D., Ağaoğulları, D., & Öveçoğlu, M. L. (2019). Room-temperature synthesis of tungsten silicide powders using various initial systems. *International Journal of Refractory Metals and Hard Materials*, 82, 58-68.
- [36] Guo, W. M., & Zhang, G. J. (2009). Reaction processes and characterization of ZrB₂ powder prepared by boro/carbothermal reduction of ZrO₂ in vacuum. *Journal of the American Ceramic Society*, 92(1), 264-267.
- [37] Akgün, B., Çamurlu, H. E., Topkaya, Y., & Sevinç, N. (2011). Mechanochemical and volume combustion synthesis of ZrB₂. *International Journal of Refractory Metals and Hard Materials*, 29(5), 601-607.
- [38] Balcı, Ö., Ağaoğulları, D., Öveçoğlu, M. L., & Duman, İ. (2016). Synthesis of niobium borides by powder metallurgy methods using Nb₂O₅, B₂O₃ and Mg blends. *Transactions of Nonferrous Metals Society of China*, 26(3), 747-758.